

# Stability of SQG Kolmogorov Flow

Mac Lee<sup>a</sup>, Stefan G. Llewellyn Smith<sup>b,c</sup>

<sup>a</sup>*Department of Physics University of California San Diego CA 92093-0319 USA*

<sup>b</sup>*Department of Mechanical and Aerospace Engineering Jacobs School of Engineering University of California San Diego CA 92093-0411 USA*

<sup>c</sup>*Scripps Institution of Oceanography University of California San Diego CA 92093-0209 USA*

---

## Abstract

Stability analysis is performed on surface quasigeostrophic systems subjected to a Kolmogorov-type “shear force” on the boundaries using linear and nonlinear approaches. For a SQG system of semi-infinite depth forced on the upper boundary, the most linearly unstable mode is 2.74 the energy injection length scale. This is contrary to two-dimensional fluid systems, where the linear instability is greatest for long waves. In the presence of damping, the most linearly unstable mode shifts toward shorter length scales. The nonlinear critical Reynolds number across different damping strengths is found to be qualitatively similar to that of Euler 2D systems. For an SQG system of finite thickness being forced on both boundaries, its behaviour approaches that of a semi-infinite SQG system at the large thickness limit. In the small thickness limit, the behaviour of a symmetrically forced fluid layer approaches that of a 2D system, while an antisymmetrically forced fluid layer is not susceptible to both linear and nonlinear instabilities. With ageostrophic effects, an SQG+ system of semi-infinite depth is much more prone to instabilities than an otherwise identical SQG system in the absence of damping due to the instability of long-wave modes. However, damping significantly suppresses such instabilities. With increasing damping, the most linearly unstable mode moves toward a smaller length scale. Contrary to the zero damping case, when the damping is sufficiently large, ageostrophic effects have a small but measurable stabilising effect.

*Keywords:* Surface quasigeostrophy, submesoscale, stability, energy method, Rossby number

---

## 1. Introduction

First proposed by [1], SQG theory was suggested by a few studies [2, 3, 4] to be a possible model to relate observable sea surface height to internal dynamics of the upper ocean in the submesoscale. [3] argued that the balanced flow resulting from SQG strongly anticorrelated with the balanced flow from QG in the upper ocean, and the overall dynamics is dominated by the SQG component. However, in the mid-latitudes, the Rossby number is not vanishingly small in the submesoscale, and SQG theory does not account for the presence of ageostrophic dynamics in this length scale. Since SQG theory consists of the first order terms of a perturbation expansion in the Rossby number, it is useful to consider next order correction terms to capture such dynamics. Such correction terms for QG were derived by [5]. In Muraki’s theory, the QG streamfunction is replaced by a vector potential, with the components governed by three Poisson equations. An ansatz given in a follow-up study which applied the same idea to SQG effectively transforms the next order equations for SQG from Poisson equations to Laplace equations [6]. Inverting these equations, one can derive diagnostic expressions of the correction terms in terms of the SQG streamfunction.

To cast light on the physical properties of SQG dynamics, the natural first step is to study known, exactly solvable configurations. Kolmogorov flow is one such configuration. In Kolmogorov flows, a viscous fluid is forced by a sinusoidal body force at one length scale, and this injection of energy is balanced by dissipation. This is one of the simplest settings in which different flow properties can be explored. Two-dimensional Kolmogorov flow has been successfully realised in laboratory experiments [7, 8]. Theoretically, the stability of this class of problem has been studied using various techniques [9, 10, 11, 12, 13]. The usual first step is to study the linearised stability problem. The

---

*Email addresses:* ma1004@ucsd.edu (Mac Lee), sg1s@ucsd.edu (Stefan G. Llewellyn Smith)

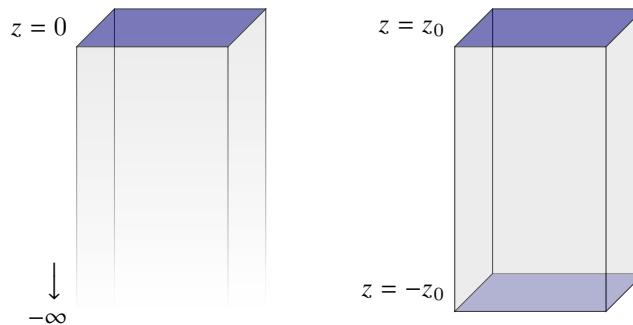


Figure 1: Illustration of the chosen system configurations. The first figure is semi-infinite, the second has finite depth.

critical Reynolds number for such a system, computed using the continued fraction method, is  $\sqrt{2}$  [9]. Further studies have been carried out on the effects of the  $\beta$ -plane [14, 15], Ekman drag [16, 15], and buoyancy [17]. However, linear analysis is only valid when the flow is slightly disturbed from the basic state. Even then, it only provides an upper bound to stability: just because a configuration has a Reynolds number below the predicted critical Reynolds number does not guarantee the stability of the configuration. To get a complementary picture of the stability properties, the energy method can be used with the nonlinear equation to obtain a lower bound for the critical Reynolds number, below which the system is guaranteed to be stable [16, 18, 15]. There have been studies of SQG Kolmogorov flows using Galerkin methods [19, 20], so that the stability of a heavily truncated system is considered, but an analysis of SQG Kolmogorov flow stability for linear and energy stability does not appear to have been carried out. With these tools, we are able to reuse the machinery developed for two-dimensional Kolmogorov flow in prior studies to study order Rossby effects in SQG+.

In this study, we choose to focus on two specific configurations. The first configuration is a semi-infinite fluid layer driven at the upper boundary. This configuration is a very simple idealisation of the upper ocean, where the upper boundary is the air-sea interface. The second configuration is a finite fluid layer that is driven at both the upper and lower boundaries with fluid below it. This is a more detailed model of the upper ocean, where the mixed layer is bounded on top by the sea surface and on the bottom by the thermocline. The mixed layer is forced on both boundaries by air-sea interaction on top and interactions between the mixed layer and the stratified layer below. These configurations are illustrated in Figure 1.

In the following sections, we carry out stability analyses using linearisation and the energy method for the SQG problem. § 2 gives a brief discussion of the SQG formulation of the Kolmogorov problem. In § 3.1, we study the linear instability of a semi-infinite system with a constant Brunt-Väisälä frequency driven at the upper boundary. This is followed by a study of the linear instability of a finite-depth system in § 3.2. The behaviours of both symmetric and antisymmetric forcing are studied. In § 4.2 and § 4.3, we study the nonlinear stability problems of the same configurations using the energy stability method. In § 5, we include  $O(\epsilon)$  corrections in the linear stability analysis or the semi-infinite configuration. § 6 concludes the paper.

## 2. Formulation of the Problem

The governing equations for an SQG system on the upper boundary of a fluids occupying  $z < 0$  are similar to those of a two-dimensional fluid system, with the relation between streamfunction and the active scalar changing. An SQG system for the upper and lower boundaries of fluid layer with  $z \in [-z_0, z_0]$  should behave like a semi-infinite SQG system in the limit of large fluid layer thickness, and like a two-dimensional system in the small thickness limit. This is because the effect of boundary forcing decreases exponentially with distance, so that as the thickness of the fluid is increased, the dynamics of the fluid close to the boundaries will be increasingly dominated by the closest boundary, effectively turning the system into two decoupled semi-infinite SQG systems. Conversely, if the forcing on the two boundaries is symmetric, the forcings from both boundaries act in concert, and their combined effect in the fluid

interior becomes increasingly less dependent on  $z$  as the thickness is reduced, effectively reducing the system into a 2D system.

The active scalar in SQG is the surface potential temperature  $\theta = \partial\psi/\partial z$ , where  $\psi$  is the streamfunction. The time evolution of the tracer is governed by the nondimensional advection equation of  $\theta$  [16, 5]:

$$\frac{\partial\theta}{\partial t} + \mathbf{u} \cdot \nabla\theta = -\frac{1}{Re_n} [(-1)^n \Delta^n \theta + \lambda\theta] + F, \quad (1)$$

where  $Re_n = UL^{2n-1}/\nu$  is the Reynolds number;  $n$  is the hyperdiffusion index, which governs the scales at which diffusion takes effect ( $n = 1$  is regular viscosity),  $\lambda$  is linear drag or (radiative) damping scaled with the Reynolds number,  $\Delta \equiv \nabla^2 = \partial^2/\partial x^2 + \partial^2/\partial y^2$  is the horizontal Laplacian, and  $F$  is a source/sink term. In Kolmogorov flow, the forcing  $F(y, z)$  is a periodic function of  $y$ . There is a laminar basic state with a balance between the energy injection at the boundary and dissipation. In SQG, the internal potential vorticity is zero,

$$\nabla_3^2 \psi = 0, \quad (2)$$

where  $\nabla_3^2 = \partial^2/\partial x^2 + \partial^2/\partial y^2 + \partial^2/\partial z^2$  is the three-dimensional Laplacian.

### 3. SQG Linear Instability

#### 3.1. Semi-infinite depth fluid

The laminar stationary solution with vanishing potential vorticity is

$$\Psi(y, z) = \Psi_0 e^z \sin y, \quad (3a)$$

from which we obtain the potential temperature function of the basic state,

$$\Theta(y, z) = \Psi_0 e^z \sin y. \quad (3b)$$

This corresponds to the forcing

$$F = \frac{\Psi_0}{Re_n} (\lambda + 1) e^z \sin y. \quad (4)$$

To examine linear disturbances to this basic state, we write

$$\psi = \Psi + \tilde{\psi} \quad \theta = \Theta + \tilde{\theta}, \quad (5)$$

where  $\tilde{\psi}$  and  $\tilde{\theta}$  are disturbance terms. This leads to the exact equation on the surface

$$\frac{\partial\tilde{\theta}}{\partial t} + J(\tilde{\psi}, \tilde{\theta}) + \Psi_0 (\tilde{\theta} + \tilde{\psi})_x \cos y = -\frac{1}{Re_n} \{(-1)^n \Delta^n + \lambda\} \tilde{\theta}, \quad (6)$$

where  $f_x = \partial f/\partial x$  and the Jacobian is given by  $J(f, g) = f_x g_y - f_y g_x$ . To obtain the growth rate of the unstable states, we substitute a Floquet ansatz

$$\tilde{\psi}(x, y, z, t) = e^{\sigma t + ikx + il y} \sum_{m=-\infty}^{\infty} \psi_m e^{imy + \kappa_m z}, \quad (7)$$

into (6), writing  $\kappa_n = \sqrt{k^2 + (l+n)^2}$ . When the disturbance is small, the nonlinear term  $J(\tilde{\psi}, \tilde{\theta})$  in (6) can be neglected. Substituting these equations into the linearised advection equation for  $\theta$  at the upper boundary, we obtain

$$\frac{ik\Psi_0}{2} \frac{\kappa_{m+1} - 1}{\kappa_m} \psi_{m+1} - \frac{1}{Re_n} (\kappa_m^{2n} + \lambda) \psi_m + \frac{ik\Psi_0}{2} \frac{\kappa_{m-1} - 1}{\kappa_m} \psi_{m-1} = \sigma \psi_m. \quad (8)$$

This infinite set of coupled equations is formally an infinite matrix eigenvalue problem. It can be solved numerically by truncating the sum to  $-N \leq m \leq N$ . In tests, we found no noticeable difference between  $N = 64$  and  $N = 16$ . For

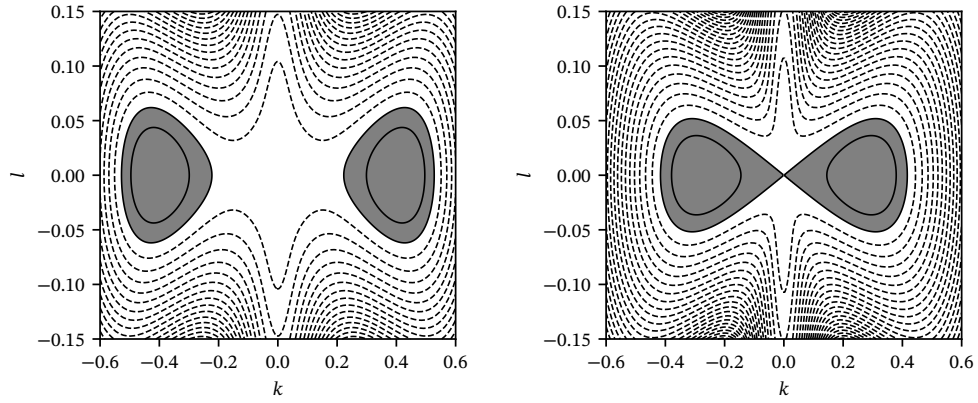


Figure 2: Left: real part of the growth rate at  $Re_n = 5.02$ . Dotted contours indicate a negative growth rate  $\sigma$ , solid contours indicate a positive growth rate. Right: analogous plot for a two-dimensional system at  $Re_n = 1.83$ . The Reynolds numbers are chosen so that the regions of instability are equal in size. In both plots,  $n = 1$  and  $\lambda = 0$ .

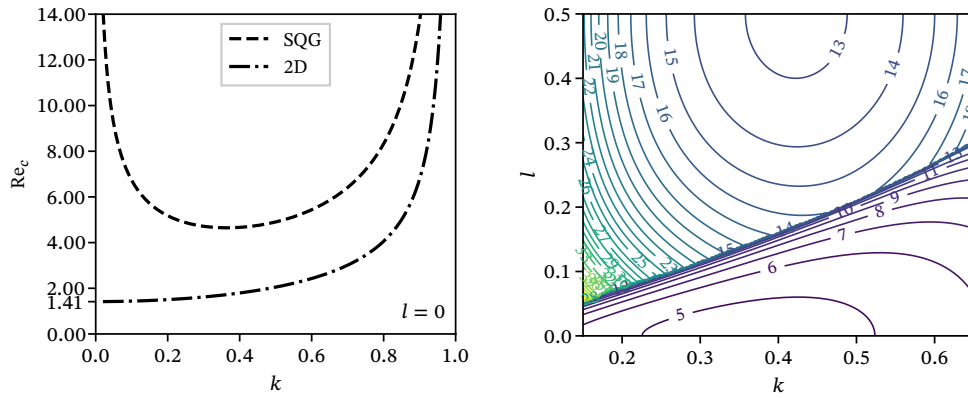


Figure 3: Left: critical Reynolds number as a function of  $k$  and  $l = 0$  with  $n = 1$  and  $\lambda = 0$ , corresponding to the smallest critical Reynolds number. Right: critical Reynolds number as a function of the wavenumbers  $k$  and  $l$ .

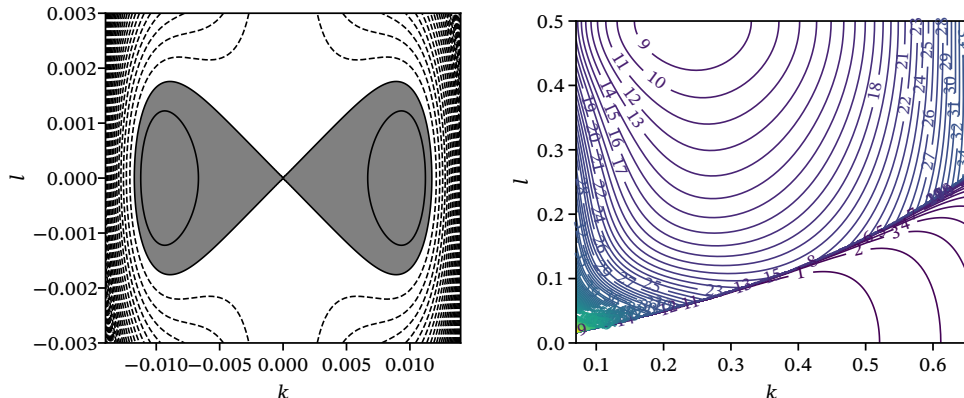


Figure 4: Left panel: growth rate for hyperdiffusion parameter  $n = 4$  with Reynolds number  $Re_n = 3 \times 10^{-5}$ ;  $\sigma > 0$  in the grey region. Right panel: contour map of critical Reynolds numbers for  $n = 4$  and  $\lambda = 0$ .

the remainder of the paper,  $N$  is 16 unless otherwise specified. At  $\lambda = 0$ , with  $\Psi_0 = 1$  and  $n = 1$ , we find that the critical Reynolds number is 4.64671 numerically, corresponding to  $l = 0$ .

Figure 2 shows that, at  $Re_1 = 5.02$ , taken to be an illustrative value showing the form of the instability region. A region of instability emerges at line  $l = 0$  near  $k = 0.36$ . The region of instability is disconnected from  $(k, l) = (0, 0)$ . This is different from a similar plot of a two-dimensional system where the instability occurs at  $k = l = 0$  in the long-wave limit and  $Re_1 = \sqrt{2}$ . This can be further illustrated by plotting the critical Reynolds number as a function of  $k$  along  $l = 0$ , as shown in Figure 3. In a two-dimensional system, with ordinary diffusion, the minimum critical Reynolds number corresponds to the mode at  $k = l = 0$ , whereas the critical Reynolds number is infinite at the same point in a semi-infinite SQG system. This indicates that in two-dimensional systems, modes with large length scale are the least stable, whereas such modes are linearly stable in SQG systems. In both systems, the critical Reynolds number approaches infinity at  $k = 1$ , and the modes at  $k > 1$  are linearly stable. Modes smaller than the length scale of energy injection are linearly stable in both Euler 2D and semi-infinite SQG. It is also helpful to visualise the critical Reynolds number as a contour plot in the horizontal wave numbers  $k$  and  $l$ , as in Figure 3. These plots show that local interactions play a more important role in SQG dynamics than in 2D dynamics.

As the hyperdiffusive parameter  $n$  increases to 4, the region of instability in wavenumber space once again connects to the origin of the plane, as shown in Figure 4. Compared to regular diffusion, hyperdiffusion more selectively suppresses small scale wave modes, enabling the large scale wave modes to once again determine the linear instability of the system. This mechanism is also much less efficient at removing energy, which manifested in a dramatic drop in the critical Reynolds number down to  $Re_c = 2.01055 \times 10^{-5}$ .

Figure 5 shows the growth rate diagram with increasing  $\lambda$ , with the Reynolds numbers just above the critical number at the given damping. The critical Reynolds number increases with damping. This relationship is shown in Figure 6. Since damping removes energy from the system across length scales, increasing damping decreases the linear instability of the system. The region of instability shifts to higher  $k$  values as  $\lambda$  is increased. The regions of instability also get more stretched in the  $l$  direction. This relationship is further illustrated with a plot of the most unstable wave mode  $k_c$  as a function of  $\lambda$ , as shown in Figure 6. Without damping, the point at  $k_c = 0.364$  is the most linearly unstable mode. As damping increases, this point shifts toward larger wavenumbers and saturates at around  $k_c = 0.650$ . The curve for a two-dimensional system is shown for comparison. Physical damping is defined by  $\lambda/Re$  with respect to the notation in (1). As physical damping increases, the removal of energy exceeds the injection of energy beyond a certain threshold, and the system can no longer become linearly unstable. In other words, the linear critical Reynolds number becomes infinity. This is shown graphically in Figure 7. For an SQG system, this threshold is at  $\lambda/Re_c = 0.119$ , which is considerably lower than that of an otherwise identical Euler 2D system. The most unstable wave mode cannot move beyond  $k_c = 0.650$  with increasing physical damping because the system ceases to be linearly unstable beyond that point. In short, SQG Kolmogorov systems are less linearly unstable than 2D systems,

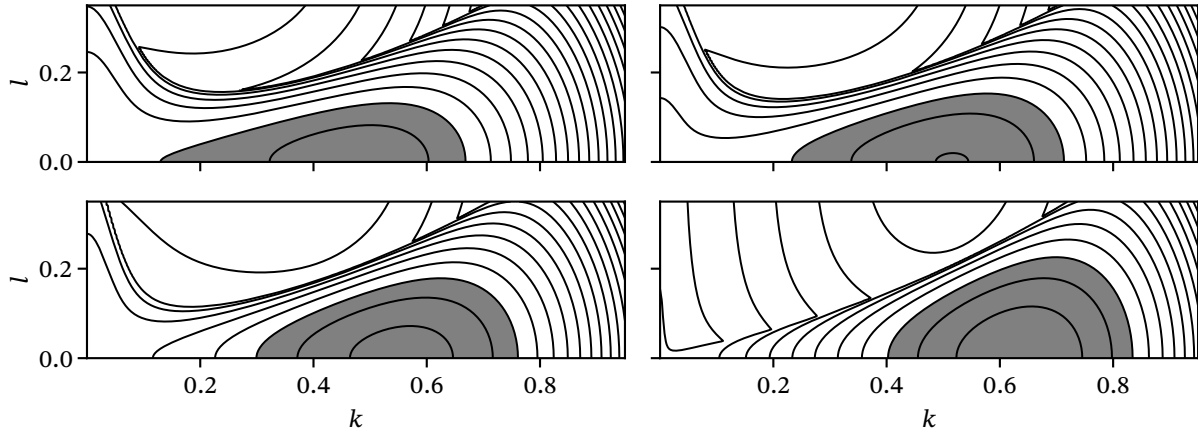


Figure 5: Growth rate diagrams for semi-infinite SQG at  $n = 1$  and  $1.3Re_c(\lambda)$ . From left to right, top to bottom,  $\lambda$  is 0, 0.05, 0.2, 5. The contour spacing is 0.01.

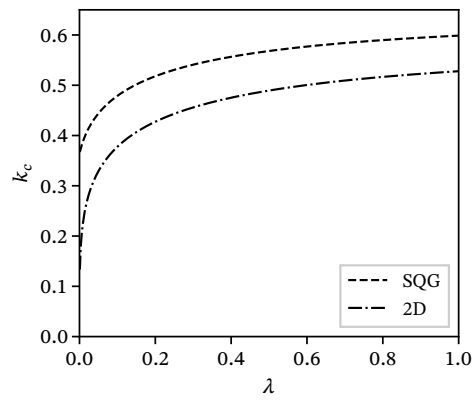


Figure 6: Plot of the critical wavenumber  $k_c$  as a function of damping  $\lambda$ . A plot of a two-dimensional curve is shown for comparison.  $k_c$  saturates at 0.650 in SQG.

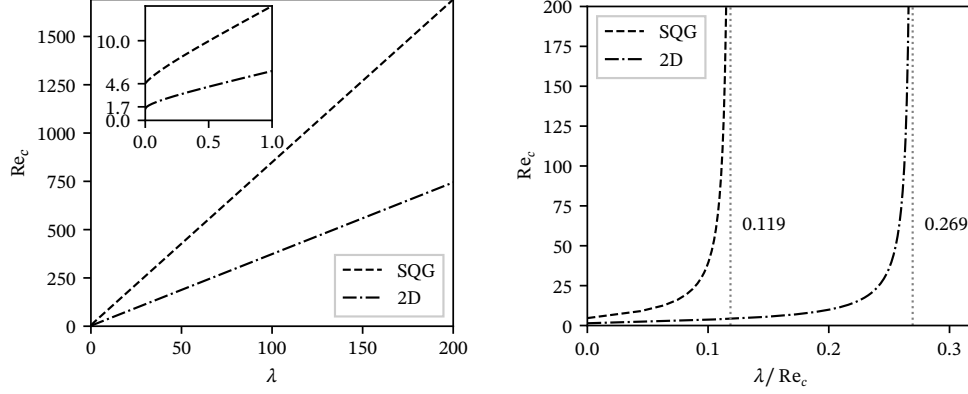


Figure 7: The first plot shows the critical Reynolds number as a function of the damping parameter  $\lambda$ . The second plot shows the critical Reynolds number as function of physical damping  $\lambda/Re_c$ .

and the linear instabilities also tend to be associated with smaller length-scales.

### 3.2. Boundary driven finite-depth fluid

In a model driven on two boundaries by Kolmogorov type forcing, the basic state can be trivially generalised from the basic state in the previous section. For mathematical simplicity, we place the two boundaries at  $z = \pm z_0$ . The configuration is visualised by the second illustration in Figure 1. The basic state is then a linear combination of two basic states corresponding to the two boundaries. We study the stability of such a system by looking at the symmetric and antisymmetric configurations separately.

We start by taking a look at the symmetric configuration. Adding the basic states on the two boundaries, the symmetric basic state in the bulk between the two boundaries is

$$\Psi(y, z) = 2\Psi_0 e^{z_0} \cosh z \sin y, \quad (9a)$$

$$\Theta(y, z) = 2\Psi_0 e^{z_0} \sinh z \sin y. \quad (9b)$$

This basic state is maintained by the forcing at the boundary,

$$F = \frac{2\Psi_0}{Re_n} (\lambda + 1) e^{-z_0} \sinh z \sin y. \quad (10)$$

On the boundaries, we require that  $w = 0$ . Using (9), the advection equation (6) becomes

$$\frac{\partial \tilde{\theta}}{\partial t} + 2\Psi_0 e^{-z_0} \left( \tilde{\theta} \cosh z_0 \pm \tilde{\psi} \sinh z_0 \right)_x \cos y = -\frac{1}{Re_n} \{(-1)^n \nabla^{2n} + \lambda\} \tilde{\theta} \quad (11)$$

at  $z = \pm z_0$  after linearisation. Using the Floquet ansatz

$$\tilde{\psi}(x, y, z, t) = e^{ikx + ily + \sigma t} \sum_{m=-\infty}^{\infty} \psi_m(z) e^{imy}, \quad (12)$$

(11) becomes

$$\begin{aligned} \{\sigma + \kappa_m^{2n} + \lambda\} \psi_m(z) \\ = ik\Psi_0 e^{-z_0} \{[\psi_{m+1}(z) + \psi_{m-1}(z)] \cosh z_0 \mp [\psi_{m+1}(z) \pm \psi_{m-1}(z)] \sinh z_0\}. \end{aligned} \quad (13)$$

By definition, the QG potential vorticity is zero in the fluid interior in SQG. The streamfunction must be a solution of Laplace's equation. Consequently, the  $z$ -dependence must assume the form

$$\psi_m(z) = \mu_m \cosh \kappa_m z + \nu_m \sinh \kappa_m z, \quad (14)$$

where  $\mu_m$  and  $\nu_m$  are coefficients to be determined. Combining (13) and (14) and evaluating at  $z = \pm z_0$ , we obtain the recurrence relation for the symmetric modes,

$$\begin{aligned} \sigma \mu_m = & - \frac{ik \Psi_0 e^{-z_0} (\kappa_{m+1} \sinh \kappa_{m+1} z_0 \cosh z_0 - \sinh z_0 \cosh \kappa_{m+1} z_0)}{\kappa_m \sinh z_0 \kappa_m} \mu_{m+1} \\ & - \frac{ik \Psi_0 e^{-z_0} (\kappa_{m-1} \sinh \kappa_{m-1} z_0 \cosh z_0 - \sinh z_0 \cosh \kappa_{m-1} z_0)}{\kappa_m \sinh z_0 \kappa_m} \mu_{m-1} \\ & - \frac{\lambda + \kappa_m^{2n}}{Re_n} \mu_m. \end{aligned} \quad (15a)$$

Similarly, the recurrence relation for the antisymmetric modes is

$$\begin{aligned} \sigma \nu_m = & - \frac{ik \Psi_0 e^{-z_0} (\kappa_{m+1} \cosh z_0 \cosh z_0 \kappa_{m+1} - \sinh z_0 \sinh \kappa_{m+1} z_0)}{\kappa_m \cosh z_0 \kappa_m} \nu_{m+1} \\ & - \frac{ik \Psi_0 e^{-z_0} (\kappa_{m-1} \cosh z_0 \cosh \kappa_{m-1} z_0 - \sinh z_0 \sinh \kappa_{m-1} z_0)}{\kappa_m \cosh z_0 \kappa_m} \nu_{m-1} \\ & - \frac{\lambda + \kappa_m^{2n}}{Re_n} \nu_m. \end{aligned} \quad (15b)$$

For the antisymmetric configuration, the streamfunction and surface potential temperature of the basic state are

$$\Psi(y, z) = 2\Psi_0 e^{z_0} \sinh z \sin y \quad (16a)$$

$$\Theta(y, z) = 2\Psi_0 e^{z_0} \cosh z \sin y. \quad (16b)$$

Taking similar steps as for the symmetric configuration, the recurrence relations for symmetric and antisymmetric modes are

$$\begin{aligned} \sigma \mu_m = & - \frac{ik \Psi_0 e^{-z_0} (\kappa_{m+1} \sinh z_0 \cosh \kappa_{m+1} z_0 - \sinh \kappa_{m+1} z_0 \cosh z_0)}{\kappa_m \sinh \kappa_m z_0} \nu_{0m+1} \\ & - \frac{ik \Psi_0 e^{-z_0} (\kappa_{m-1} \sinh z_0 \cosh \kappa_{m-1} z_0 - \sinh \kappa_{m-1} z_0 \cosh z_0)}{\kappa_m \sinh z_0 \kappa_m} \nu_{0m-1} \\ & - \frac{\lambda + \kappa_m^{2n} \mu_m}{Re_n}, \end{aligned} \quad (17)$$

$$\begin{aligned} \sigma \nu_m = & - \frac{ik \Psi_0 e^{-z_0} (\kappa_{m+1} \sinh z_0 \sinh \kappa_{m+1} z_0 - \cosh z_0 \cosh \kappa_{m+1} z_0)}{\kappa_m \cosh z_0 \kappa_m} \mu_{0m+1} \\ & - \frac{ik \Psi_0 e^{-z_0} (\kappa_{m-1} \sinh z_0 \sinh \kappa_{m-1} z_0 - \cosh z_0 \cosh \kappa_{m-1} z_0)}{\kappa_m \cosh z_0 \kappa_m} \mu_{0m-1} \\ & - \frac{\lambda + \kappa_m^{2n}}{Re_n} \nu_m. \end{aligned} \quad (18)$$

The growth rate diagrams for both the symmetrically and antisymmetrically forced system are shown in Figure 8. The region of instability of the symmetrically forced system is noticeably bigger than the antisymmetrically forced system for the chosen  $z_0$  and  $Re_n$ . This behaviour is due to the critical Reynolds number being slightly lower in the symmetric configuration than the antisymmetric configuration at this separation distance  $z_0$ . The relationship of the critical Reynolds number with  $z_0$  is shown in Figure 9. When  $z_0 \gg 1$ , critical Reynolds number asymptotically

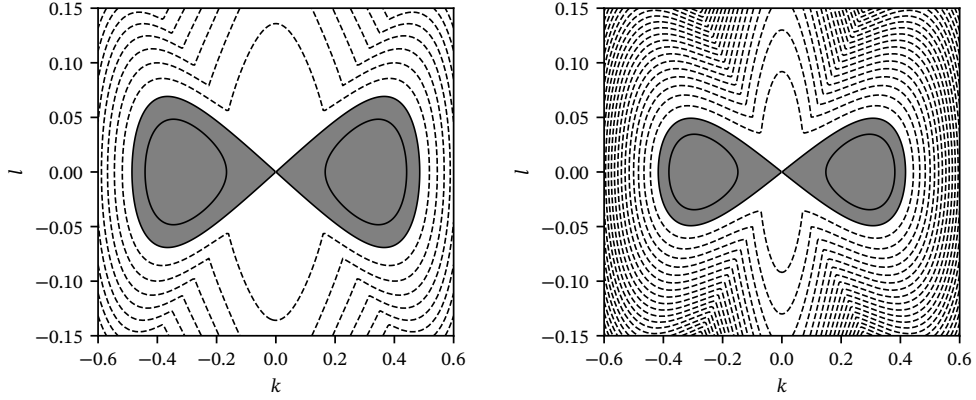


Figure 8: Left panel: real part of the growth rate of the linearised system for a symmetric configuration, similar to Figure 2. The growth rate is positive in the grey region. This plot corresponds to  $z_0 = 2.2$  and  $Re_n = 3.8$ . Right: the growth rate plot for the antisymmetric configuration with identical parameters. The unstable region in  $k$ - $l$  space is enlarged with the symmetric configuration compared to the antisymmetric configuration.

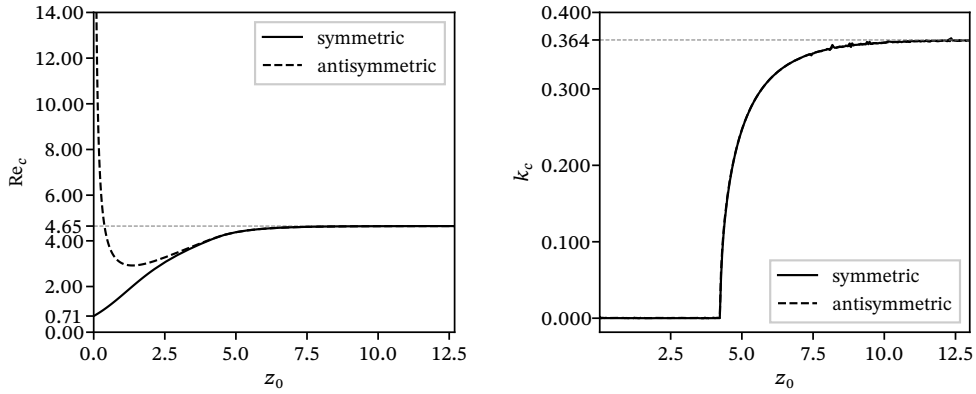


Figure 9: Left panel: critical Reynolds number  $Re_c$  vs.  $z_0$ . The horizontal line indicates  $Re_n = 4.6467$ . The critical Reynolds number for symmetric forcing increases monotonically until it saturates at around  $Re_n = 4.6467$ . With antisymmetric forcing, the critical Reynolds number is infinite at  $z_0 = 0$  and then rapidly decreases. The neutral line of antisymmetric forcing asymptotically converges to that of symmetric forcing. Right panel: the corresponding horizontal wavenumber  $k$ . At low separation distances, the wavenumber corresponding to the most unstable mode  $k_c$  is identically zero, as it is in a two-dimensional system. At a separation distance larger than 4.22,  $k_c$  moves outward on the  $k$ -axis and approaches  $k_c = 0.3640$ , which corresponds to  $k_c$  in semi-infinite SQG.

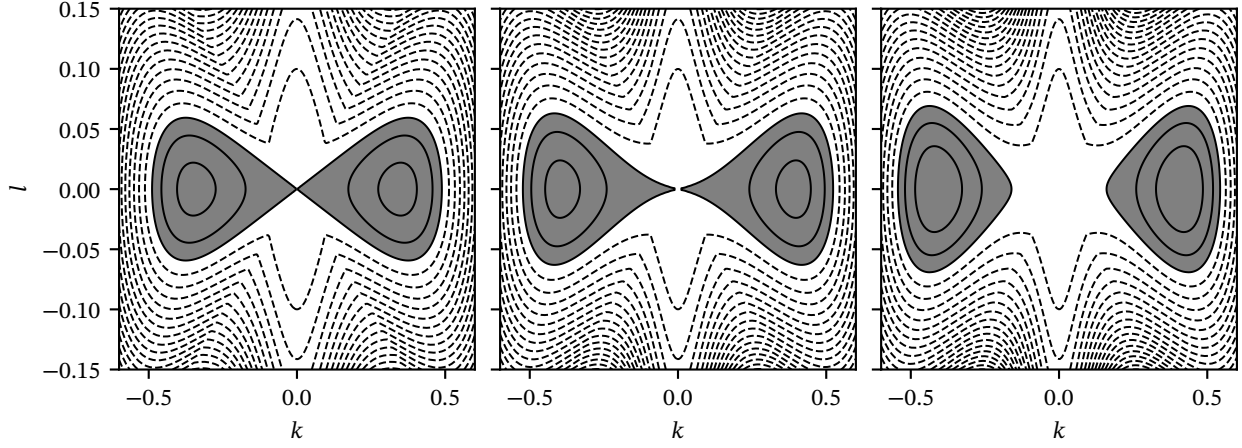


Figure 10: Growth rate diagrams at  $z_0$  at 4, 6, 8 and  $Re_n$  at 4.67, 4.978 and 5.092 for symmetric forcing. The Reynolds numbers were chosen to produce diagrams with regions of instability with the same size.  $\lambda = 0$ ,  $n = 1$ ,  $N = 16$ . At small separation distances, the growth rate diagram resembles that of a two-dimensional system; at large separation distances, the growth rate diagram resembles that of an SQG system with a semi-infinite layer.

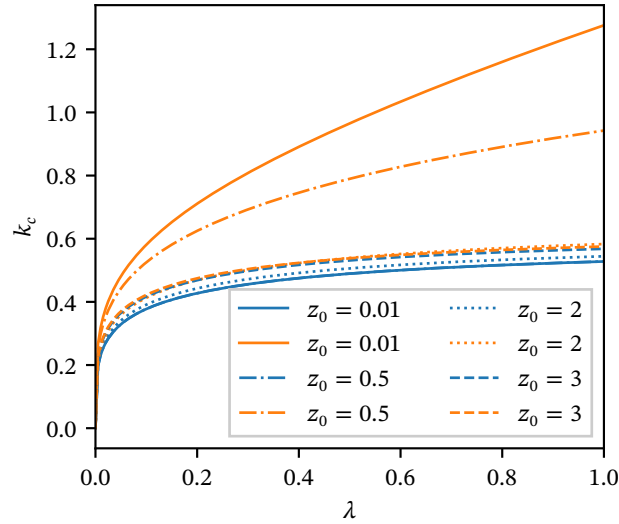


Figure 11: Critical wavenumber  $k_c$  as a function of damping  $\lambda$  at various separation distances. The orange (blue) curves corresponds to the (anti)symmetric configuration.

approaches the value obtained for SQG in the semi-infinite fluid layer in § 3.1. When  $z_0 \ll 1$ , the critical Reynolds numbers of these two configurations diverge, with  $Re_c$  becoming infinity for the antisymmetric configuration at  $z_0 = 0$ . The critical Reynolds number for the symmetric configuration becomes  $1/\sqrt{2}$  when  $z_0$  approaches 0. The specific effect of layer thickness in a boundary driven finite-thickness SQG system on the growth rate diagram can be seen in Figure 10. At low  $z_0$ , the regions have a teardrop shape and are connected to the origin of the  $k$ - $l$  plane. The regions of instability are connected to the origin even when the Reynolds number is only slightly above  $Re_c$ , just as it is in a two-dimensional system. As  $z_0$  is increased, the teardrop-shaped regions of instability retreat toward higher  $|k|$  when the Reynolds number is slightly above  $Re_c$ , indicating the point in wavenumber space that first gets unstable shifts to larger  $|k|$  as the fluid layer thickness is increased. The panel on the right resembles that of the semi-infinite SQG system. This behaviour is further illustrated by plotting the critical wavenumber  $k_c$  against  $z_0$ , as shown in the right panel of Figure 9. At small  $z_0$ , the most linearly unstable state corresponds to the long-wave limit. This resembles the behaviour of a two-dimensional system. However, as the layer thickness is increased beyond about  $z_0 = 4.3$ , the most unstable mode abruptly shifts away from the two-dimensional value and stabilises at  $k_c = 0.364$ , the semi-infinite SQG value. This can be explained from the recurrence relation itself. At the large separation limit, both (15a) and (15b) reduce to

$$\sigma_0 e^{\kappa_m z_0} \Psi_{0m} = -\frac{ik\Psi_0}{2} \frac{\kappa_{m+1} - 1}{\kappa_m} e^{\kappa_{m+1} z_0} \Psi_{0m+1} - \frac{ik\Psi_0}{2} \frac{\kappa_{m-1} - 1}{\kappa_m} e^{\kappa_{m-1} z_0} \Psi_{0m-1} - \frac{\lambda + \kappa_m^{2n}}{Re_n} e^{\kappa_m z_0} \Psi_{0m}. \quad (19)$$

When  $k$  or  $l$  is sufficiently big,  $\kappa_m \sim \kappa_{m\pm 1}$ , and this equation reduces to (56). We can expect the small length scale modes to behave very similarly to that of a semi-infinite SQG system. At the small  $z_0$  limit, (15a) reduces to

$$\sigma \mu_m = -\frac{ik\Psi_0(\kappa_{m+1}^2 - 1)}{\kappa_m^2} \mu_{m+1} - \frac{ik\Psi_0(\kappa_{m-1}^2 - 1)}{\kappa_m^2} \mu_{m-1} - \frac{\lambda + \kappa_m^{2n}}{Re_n} \mu_m. \quad (20)$$

Comparing this with (8) confirms that the critical Reynolds number at this limit is  $1/\sqrt{2}$ .

## 4. SQG Nonlinear Stability

### 4.1. The energy method

Linear stability analysis gives the critical Reynolds number above which small disturbances grow. However, since the instability conditions are obtained under the assumption of small perturbations of the basic state, the actual threshold for instability could be much lower. To find an accurate picture of the line across which stability is guaranteed, we need to take into account nonlinear effects. We adapt the nonlinear stability analysis approach taken by [16] for SQG. The discussion is supplemented by [18] and [15]. We start by noting that the kinetic energy, as it is conventionally defined, can be written in terms of potential temperature through Parseval's theorem if the horizontal boundaries are periodic, with

$$E \equiv -\frac{1}{2} \iint_S \psi \nabla^2 \psi \, dS = \frac{1}{2} \sum_{k=-\infty}^{\infty} \sum_{l=-\infty}^{\infty} \hat{\psi}_{k,l} |\kappa|^2 \hat{\psi}_{-k,-l} \equiv \frac{1}{2} \iint_S \theta^2 \, dS, \quad (21)$$

where  $\kappa^2 = k^2 + l^2$ . We define the disturbance energy as

$$\mathcal{E} = \frac{1}{2} \iint_S \tilde{\theta}^2 \, dS. \quad (22)$$

We focus on  $n = 1$  in the remainder of this section. Using the advection equation, (6), the time evolution of disturbance energy is

$$\begin{aligned} \frac{d\mathcal{E}}{dt} &= \frac{1}{2} \frac{d}{dt} \iint_S \tilde{\theta}^2 \, dS = \iint_S \tilde{\theta} \frac{\partial \tilde{\theta}}{\partial t} \, dS \\ &= \iint_S \tilde{\theta} \left\{ \frac{1}{Re} (\Delta - \lambda) \tilde{\theta} - J(\Psi, \Theta) - J(\Psi, \tilde{\theta}) - J(\tilde{\psi}, \Theta) - J(\tilde{\psi}, \tilde{\theta}) \right\} \, dS. \end{aligned} \quad (23)$$

Since Kolmogorov flow is an equilibrium state,  $J(\Psi, \Theta) = 0$ . The integrals of the two terms  $\tilde{\theta}J(\tilde{\psi}, \tilde{\theta})$  and  $\tilde{\theta}J(\Psi, \tilde{\theta})$  can also be shown to be zero. Therefore

$$\frac{d\mathcal{E}}{dt} = \iint_S \tilde{\theta} \left\{ \frac{1}{Re} (\Delta - \lambda) \tilde{\theta} - J(\tilde{\psi}, \Theta) \right\} dS. \quad (24)$$

The equation can be rewritten as

$$\frac{d\mathcal{E}}{dt} = B - \frac{1}{Re} D, \quad (25)$$

where

$$B \equiv \iint_S \tilde{\theta} J(\Theta, \tilde{\psi}) dS \quad (26)$$

is the production term and

$$D \equiv \iint_S \tilde{\theta} (\lambda - \Delta) \tilde{\theta} dS \quad (27)$$

is the dissipation term. It will be useful to define a critical Reynolds number,

$$\frac{1}{Re_c} = \max \frac{B}{D}. \quad (28)$$

From this definition, the change of the disturbance energy over time is bounded by

$$\frac{d\mathcal{E}}{dt} \leq D \left( \frac{1}{Re_c} - \frac{1}{Re} \right). \quad (29)$$

Using the Poincaré inequality  $|\nabla \tilde{\theta}|^2 \geq C|\tilde{\theta}|^2$  where  $C$  is a constant, and integrating by parts, we obtain an upper bound for the dissipation term

$$D = \iint_S \tilde{\theta} (\lambda - \Delta) \tilde{\theta} dS = \lambda \iint_S \tilde{\theta}^2 dS + \iint_S |\nabla \tilde{\theta}|^2 dS \geq 2(\lambda + C)\mathcal{E}. \quad (30)$$

With  $Re < Re_c$ , we can combine (29) and (30) and obtain an upper bound for the rate of change of energy,

$$\frac{d\mathcal{E}}{dt} \leq 2(\lambda + C) \left( \frac{1}{Re_c} - \frac{1}{Re} \right) \mathcal{E}. \quad (31)$$

Using Gronwall's inequality, we can solve this equation and obtain an upper bound for  $\mathcal{E}$ ,

$$\mathcal{E} \leq \mathcal{E}_0 \exp \left\{ 2(\lambda + C) \left( \frac{1}{Re_c} - \frac{1}{Re} \right) t \right\}. \quad (32)$$

In other words, the disturbance energy is guaranteed to monotonically decay if  $Re < Re_c$ . The nonlinear critical Reynolds number can be obtained by maximising  $B/D$  by varying the disturbance streamfunction  $\tilde{\psi}$ ,

$$\frac{\delta(B/D)}{\delta \tilde{\psi}} = 0, \quad (33)$$

or equivalently,

$$\delta B - \frac{1}{Re} \delta D = 0. \quad (34)$$

Since  $\tilde{\psi}$  satisfies Laplace's equation, the functional variation  $\delta \tilde{\psi}$  must also satisfy Laplace's equation. Using (26), we obtain

$$\delta B = \iint_S \left\{ \frac{\partial \delta \tilde{\psi}}{\partial z} J(\tilde{\psi}, \Theta) + \frac{\partial \tilde{\psi}}{\partial z} J(\delta \tilde{\psi}, \Theta) \right\} dS. \quad (35)$$

We integrate the first term by parts,

$$\iint_S \frac{\partial \delta \tilde{\psi}}{\partial z} J(\tilde{\psi}, \Theta) \, dS \equiv i \iint_S \Delta^{1/2} (\delta \tilde{\psi}) J(\tilde{\psi}, \Theta) \, dS = i \iint_S \delta \tilde{\psi} \Delta^{1/2} J(\tilde{\psi}, \Theta) \, dS, \quad (36)$$

since for functions  $g$  and  $h$  that are doubly periodic on the domain  $S$ , it can be shown by Parseval's theorem that

$$\iint_S g \Delta^{1/2} h \, dS = \iint_S h \Delta^{1/2} g \, dS. \quad (37)$$

Here  $\Delta^{\alpha/2}$  is the fractional Laplacian defined by its effect in  $k$ -space,

$$\theta = (-\Delta)^{\alpha/2} \psi, \quad \hat{\theta}(\mathbf{k}) = |\kappa|^\alpha \hat{\psi}(\mathbf{k}), \quad (38)$$

where  $\kappa^2 = k^2 + l^2$ . In SQG,  $(-\Delta)^{1/2} \equiv \partial/\partial z$ . Integrating the second term by parts gives

$$\iint_S \frac{\partial \tilde{\psi}}{\partial z} J(\delta \tilde{\psi}, \Theta) \, dS = \iint_S \frac{\partial \tilde{\psi}}{\partial z} \left( \frac{\partial \delta \tilde{\psi}}{\partial x} \frac{\partial \Theta}{\partial y} - \frac{\partial \delta \tilde{\psi}}{\partial y} \frac{\partial \Theta}{\partial x} \right) \, dS \quad (39a)$$

$$= - \iint_S \left\{ \frac{\partial}{\partial x} \left( \frac{\partial \tilde{\psi}}{\partial z} \frac{\partial \Theta}{\partial y} \right) - \frac{\partial}{\partial y} \left( \frac{\partial \tilde{\psi}}{\partial z} \frac{\partial \Theta}{\partial x} \right) \right\} \delta \tilde{\psi} \, dS \quad (39b)$$

$$\equiv -i \iint_S J(\Delta^{1/2} \tilde{\psi}, \Theta) \delta \tilde{\psi} \, dS. \quad (39c)$$

Therefore

$$\delta B = i \iint_S \{ \Delta^{1/2} J(\tilde{\psi}, \Theta) - J(\Delta^{1/2} \tilde{\psi}, \Theta) \} \delta \tilde{\psi} \, dS. \quad (40)$$

Likewise,

$$\delta D = - \iint_S \left\{ 2\lambda \frac{\partial \delta \tilde{\psi}}{\partial z} \frac{\partial \tilde{\psi}}{\partial z} - \frac{\partial \delta \tilde{\psi}}{\partial z} \Delta \tilde{\theta} - \tilde{\theta} \Delta \frac{\partial \delta \tilde{\psi}}{\partial z} \right\} \, dS \quad (41a)$$

$$= \iint_S 2(\lambda - \Delta) \Delta \tilde{\psi} \delta \tilde{\psi} \, dS \quad (41b)$$

where we used (37). Combining (34), (40) and (41b), we have

$$\iint_S \left\{ \frac{2}{Re} (\lambda - \Delta) \Delta \tilde{\psi} - i \Delta^{1/2} J(\tilde{\psi}, \Theta) + i J(\Delta^{1/2} \tilde{\psi}, \Theta) \right\} \delta \tilde{\psi} \, dS = 0. \quad (42)$$

Since  $\delta \tilde{\psi}$  is an arbitrary function, the expression in the brackets must be zero, so

$$\frac{2}{Re} (\lambda - \Delta) \Delta \tilde{\psi} - i \Delta^{1/2} J(\tilde{\psi}, \Theta) + i J(\Delta^{1/2} \tilde{\psi}, \Theta) = 0. \quad (43)$$

To find the critical Reynolds number, we need to solve this eigenproblem.

#### 4.2. Semi-infinite depth fluid

For a semi-infinite fluid layer, we use the ansatz

$$\tilde{\psi} = e^{ikx+ily} \sum_{m=-\infty}^{\infty} \psi_m e^{imy+\kappa_m z}. \quad (44)$$

Substituting into the equation, one obtains an infinite set of coupled equations

$$\frac{1}{Re} \psi_m = \frac{ik\Psi_0}{4} \frac{\kappa_m - \kappa_{m-1}}{\kappa_m^2 (\lambda + \kappa_m^2)} \psi_{m-1} + \frac{ik\Psi_0}{4} \frac{\kappa_m - \kappa_{m+1}}{\kappa_m^2 (\lambda + \kappa_m^2)} \psi_{m+1}. \quad (45)$$

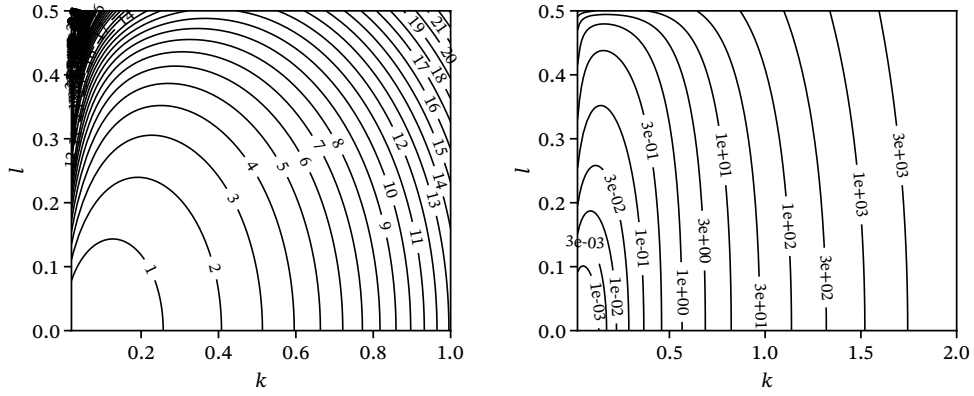


Figure 12: Critical Reynolds number using the energy method. Left: critical Reynolds number with hyperdiffusion parameter  $n = 1$ . Right: critical Reynolds number with hyperdiffusion parameter  $n = 4$ .  $\lambda = 0$  for both plots.

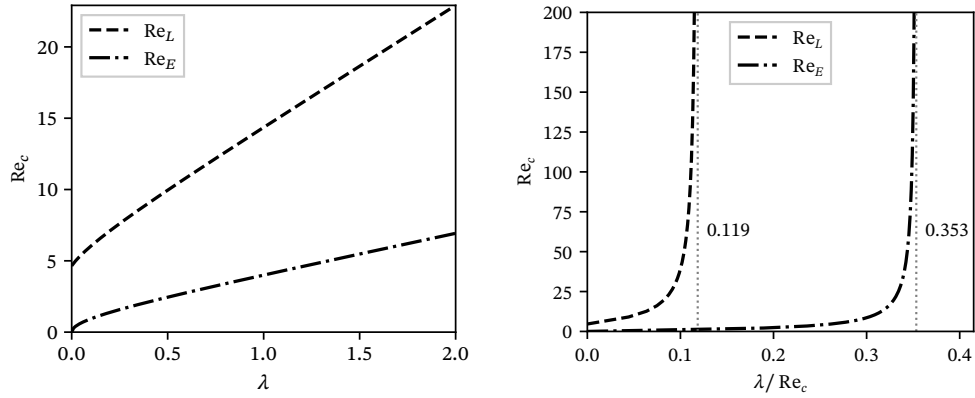


Figure 13: Variation of the critical Reynolds number  $Re_c$  with damping  $\lambda$ . Left plot: the upper line is the critical Reynolds number for linear instability; the lower line is the critical Reynolds number for nonlinear stability (we use the notation of Fukuta et al. with  $Re_L$  for the critical Reynolds number calculated by linearisation and  $Re_E$  for the critical Reynolds number calculated using the energy method). Right plot: the critical Reynolds number plotted against the unscaled drag parameter  $\lambda/Re_c$ . The asymptotes shown in the plot correspond to the slopes in the first plot as  $\lambda \rightarrow \infty$ .

We obtain the critical Reynolds number by solving the coupled equations as an eigenvalue problem numerically in the same fashion as the previous sections. The results are plotted in wavenumber space in Figure 12. With both regular diffusion and hyperdiffusion, the critical Reynolds number increases as  $k$  and  $l$  increases. In the limit of  $k \ll 1$  and  $l \ll 1$ , the critical Reynolds number is zero.

The effect of damping introduces another parameter to the analysis. As shown in Figure 13, the critical Reynolds number increases as the damping is increased. For comparison, the neutral line computed from linear instability analysis is also shown in the same plots. Since damping and diffusion compete to remove energy from the system, in the presence of damping, a higher Reynolds number is required to put the system in an unstable state. In the presence of large damping, its relationship with the linear and nonlinear critical Reynolds number appears to be linear, as shown in the right panel. The neutral line from the linear instability analysis, shown as a dashed line, lies above the line obtained through the energy method. It gives an upper bound past which the system is unstable. The neutral line obtained through the energy method gives a lower bound under which the system is guaranteed to be stable. The system is not guaranteed to be stable in the absence of damping. The nonlinear critical wavenumber  $k_c$  stays at zero even at  $\lambda = 100$ .

### 4.3. Boundary driven finite-depth fluid

For a fluid with finite thickness, we use the following Floquet ansatz:

$$\tilde{\psi} = e^{ikx+ily} \sum_{m=-\infty}^{\infty} (\mu_m \cosh \kappa_m z + \nu_m \sinh \kappa_m z) e^{imy}. \quad (46)$$

This ansatz takes into account the symmetric and antisymmetric modes of the system. As in the linear analysis, we study the symmetric and antisymmetric configuration separately.

For a symmetric configuration, we substitute the ansatz and the symmetric basic state, (9b), into (43). The recurrence relations are

$$\frac{\mu_m}{Re} = - \frac{ik\Psi_0 (\kappa_{m+1} - \kappa_m) e^{-z_0} \cosh z_0 \cosh z_0 \kappa_{m+1}}{2\kappa_m^2 (\lambda + \kappa_m^2) \cosh z_0 \kappa_m} \mu_{m+1} - \frac{ik\Psi_0 (\kappa_{m-1} - \kappa_m) e^{-z_0} \cosh z_0 \cosh z_0 \kappa_{m-1}}{2\kappa_m^2 (\lambda + \kappa_m^2) \cosh z_0 \kappa_m} \mu_{m-1} \quad (47a)$$

for the symmetric modes, and

$$\frac{\nu_m}{Re} = - \frac{ik\Psi_0 (\kappa_{m+1} - \kappa_m) e^{-z_0} \sinh z_0 \cosh z_0 \kappa_{m+1}}{2\kappa_m^2 (\lambda + \kappa_m^n) \sinh z_0 \kappa_m} \nu_{m+1} - \frac{ik\Psi_0 (\kappa_{m-1} - \kappa_m) e^{-z_0} \sinh z_0 \cosh z_0 \kappa_{m-1}}{2\kappa_m^2 (\lambda + \kappa_m^n) \sinh z_0 \kappa_m} \nu_{m-1} \quad (47b)$$

for the antisymmetric modes. Likewise, for an antisymmetric configuration, we substitute the ansatz and the antisymmetric basic state, (16b), into (43). The recurrence relations are

$$\frac{\mu_m}{Re} = - \frac{ik\Psi_0 (\kappa_{m+1} - \kappa_m) e^{-z_0} \sinh z_0 \sinh z_0 \kappa_{m+1}}{2\kappa_m^2 (\lambda + \kappa_m^n) \cosh z_0 \kappa_m} \nu_{m+1} - \frac{ik\Psi_0 (\kappa_{m-1} - \kappa_m) e^{-z_0} \sinh z_0 \sinh z_0 \kappa_{m-1}}{2\kappa_m^2 (\lambda + \kappa_m^n) \cosh z_0 \kappa_m} \nu_{m-1} \quad (48a)$$

for the symmetric modes, and

$$\frac{\nu_m}{Re} = - \frac{ik\Psi_0 (\kappa_{m+1} - \kappa_m) e^{-z_0} \sinh z_0 \cosh z_0 \kappa_{m+1}}{2\kappa_m^2 (\lambda + \kappa_m^n) \sinh z_0 \kappa_m} \mu_{m+1} - \frac{ik\Psi_0 (\kappa_{m-1} - \kappa_m) e^{-z_0} \sinh z_0 \cosh z_0 \kappa_{m-1}}{2\kappa_m^2 (\lambda + \kappa_m^n) \sinh z_0 \kappa_m} \mu_{m-1} \quad (48b)$$

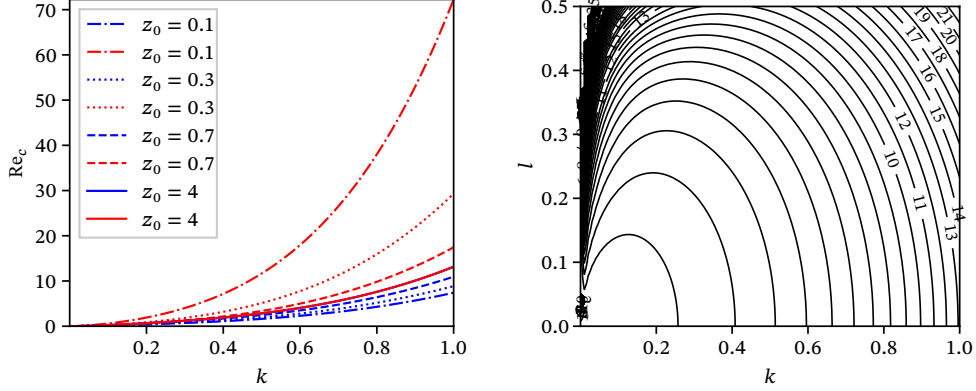


Figure 14: The left panel shows the critical Reynolds number for symmetric forcing as a function of  $k$  obtained through the energy method at  $l = 0$ . Blue (red) curves correspond to a (anti)symmetric modes. The right panel shows the critical Reynolds number for symmetric forcing as a contour map in wavenumber space.

for the antisymmetric modes.

The critical Reynolds number increases as a function of the horizontal wavenumber  $k$  for both symmetric and antisymmetric modes. The effect of the separation distance can be seen from the different behaviours between the red and blue curves in Figure 14. As the separation distance  $z_0$  is increased, the slope of  $Re_c$  with respect to  $k$  decreases for the system for antisymmetric forcing. The opposite behaviour is true for a system for symmetric forcing. In general, larger wavenumbers, or smaller length scales, are more stable than smaller wavenumbers or larger length scales.

The critical Reynolds number as a function of damping is shown in Figure 15. A system with antisymmetric forcing is more stable, linearly or nonlinearly, than a system with symmetric forcing. As the separation distance is increased, the neutral curves approach that of a semi-infinite SQG+ system, shown in 13. Both the linear and nonlinear critical Reynolds number appear to be linear functions at sufficiently large damping.  $Re_c/\lambda$  is plotted against  $z_0$  in Figure 16. Both the symmetric and antisymmetric curves converge to horizontal lines at sufficiently large  $z_0$ . The levels of these horizontal lines correspond to values in a semi-infinite SQG system.

## 5. SQG+ Linear Instability of a Semi-Infinite Layer

Studying all the configurations covered in the previous sections with order Rossby corrections using linearisation and the energy method presents numerous challenges. The study of linear instability of a layer forced on two boundaries is technically possible, but the conventional approach of finding a recurrence relation and solving with an eigenvalue solver cannot be directly applied here. One can also show that studying SQG+ nonlinear stability even for the simpler configuration of a semi-infinite layer using the correction terms derived by [5] and [6] is infeasible. For these practical considerations, for the remainder of the paper, we limit ourselves to studying only the semi-infinite layer in SQG+.

With order Rossby corrections, the existing notation used in the previous sections is no longer adequate. In SQG+, a source vector field replaces the streamfunction [5]. Using the  $\Phi$  component of the vector field as an example, we rewrite the component as a perturbation expansion in the Rossby number  $\varepsilon \equiv U/fL$ ,

$$\Phi(x, y, z, t) = \Phi^0(x, y, z, t) + \varepsilon\Phi^1(x, y, z, t) + \mathcal{O}(\varepsilon^2). \quad (49)$$

In the  $\varepsilon \ll 1$  limit, we recover  $\Phi = \Phi^0$  as the SQG streamfunction. To study the linear instability, this expansion is further expanded to account for small perturbations around a periodic basic state,

$$\Phi^0(x, y, z, t) = \Phi^{00}(y, z) + \alpha\Phi^{01}(x, y, z, t) + \mathcal{O}(\alpha^2) \quad (50a)$$

$$\Phi^1(x, y, z, t) = \Phi^{10}(y, z) + \alpha\Phi^{11}(x, y, z, t) + \mathcal{O}(\alpha^2), \quad (50b)$$

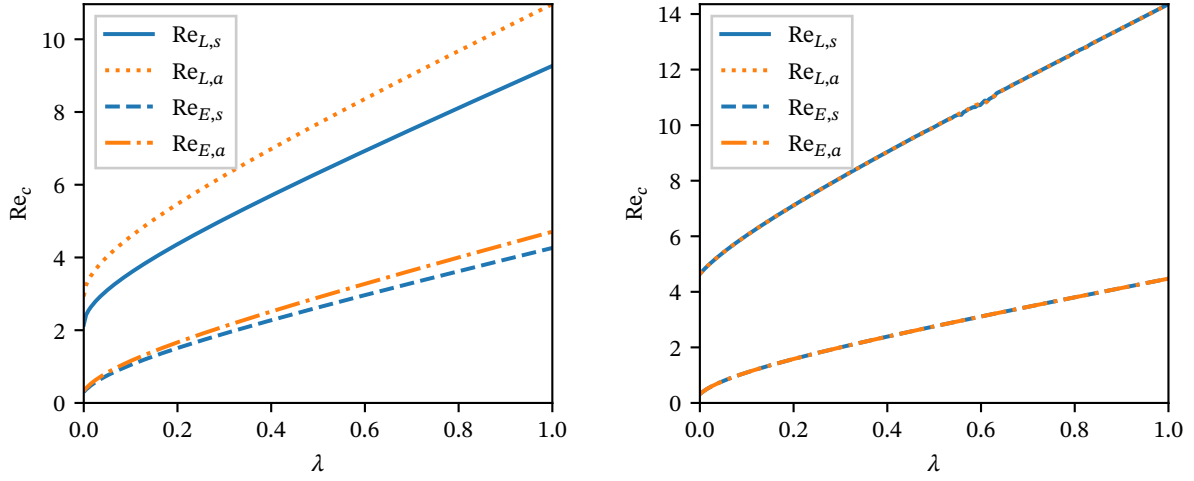


Figure 15: Critical Reynolds number vs.  $\lambda$  at two different separating distances. The first plot corresponds to  $z_0 = 1.5$ . The second plot corresponds to  $z_0 = 10$ .

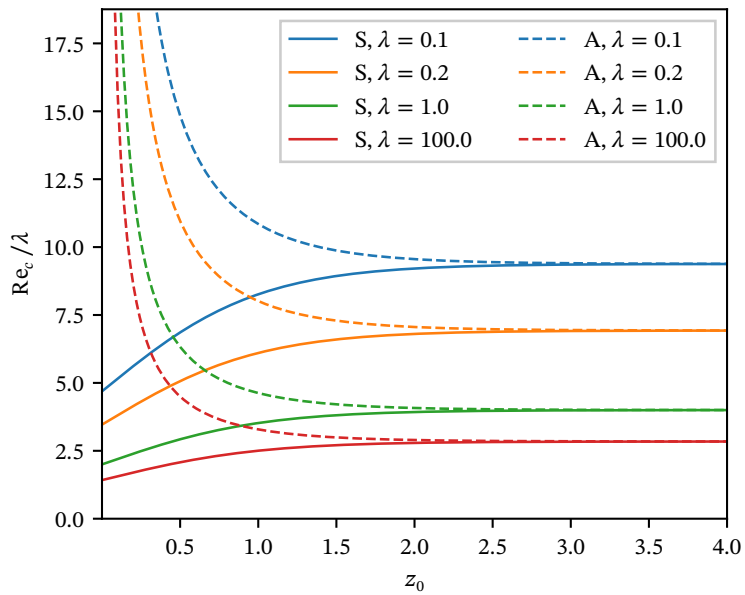


Figure 16: Critical Reynolds number vs.  $z_0$  using the energy method. Solutions form the (anti)symmetric configuration are plotted in (dashed) solid curves.

where, on the right hand side, the first digit in the superscript indicates the order in the Rossby number, and the second digit in the superscript indicates the order in the small disturbance expansion, with  $\alpha$  the magnitude of this disturbance. Combining the above, the  $\Phi$  component of the vector field can be written as

$$\Phi(x, y, z, t) = \Phi^{00}(y, z) + \varepsilon\Phi^{10}(y, z) + \alpha\Phi^{01}(x, y, z, t) + \varepsilon\alpha\Phi^{11}(x, y, z, t) + \dots \quad (51)$$

We will follow this procedure in the following passage, expanding first in the Rossby number followed by an expansion in the small disturbance limit.

Using the notation we have established, we expand the advection equation (1) in the Rossby number using (49), limiting ourselves to terms up to  $O(\varepsilon)$ ,

$$\frac{\partial}{\partial t} (\Phi_z^0 + \varepsilon\Phi_z^1) + (\mathbf{u}^0 + \varepsilon\mathbf{u}^1) \cdot \nabla (\Phi_z^0 + \varepsilon\Phi_z^1) = -\frac{1}{Re} \{(-1)^n \Delta^n + \lambda\} (\Phi_z^0 + \varepsilon\Phi_z^1) + F. \quad (52)$$

With the explicit next order correction terms derived by [5] and [6], we rewrite (52) in terms of  $\Phi^0$  and various tilde terms that will be expanded in later steps,

$$\begin{aligned} & \Phi_{zt}^0 + \varepsilon(\Phi_z^0\Phi_{zzt}^0 + \Phi_{zz}^0\Phi_{zt}^0 + \tilde{\Phi}_{zt}^1) + u(\Phi_{xz}^0 + \varepsilon(\Phi_z^0\Phi_{xzz}^0 + \Phi_{zz}^0\Phi_{xz}^0 + \tilde{\Phi}_{xz}^1)) \\ & + v(\Phi_{yz}^0 + \varepsilon(\Phi_z^0\Phi_{yzz}^0 + \Phi_{zz}^0\Phi_{yz}^0 + \tilde{\Phi}_{yz}^1)) \\ & = -\frac{(-1)^n}{Re} \Delta^n (\Phi_z^0 + (\varepsilon(\Phi_z^0\Phi_{zz}^0 + \tilde{\Phi}_z^0))) + \frac{\lambda}{Re} (\Phi_z^0 + \varepsilon(\Phi_z^0\Phi_{zz}^0 + \tilde{\Phi}_z^0)), \end{aligned} \quad (53a)$$

where

$$u = -\Phi_y^0 - \varepsilon\Phi_y^0\Phi_{zz}^0 - 2\varepsilon\Phi_z^0\Phi_{yz}^0 - \varepsilon\tilde{\Phi}_y^1 - \varepsilon\tilde{F}_z^1 \quad (53b)$$

$$v = \Phi_x^0 + \varepsilon\Phi_x^0\Phi_{zz}^0 + 2\varepsilon\Phi_{xz}^0\Phi_z^0 + \varepsilon\tilde{\Phi}_x^1 - \varepsilon\tilde{G}_z^1. \quad (53c)$$

Next, we expand using (50). The expansion is too long to be shown in full here. After the expansion, the velocity terms (53) are, up to  $O(\varepsilon)$ ,  $O(\alpha)$ , and  $O(\alpha\varepsilon)$ , with  $\kappa = \sqrt{k^2 + l^2}$ ,

$$\begin{aligned} u = & -\Phi_y^{00} - \varepsilon\Phi_y^{00}\Phi_{zz}^{00} - 2\varepsilon\Phi_z^{00}\Phi_{yz}^{00} - \alpha\Phi_y^{01} - \alpha\varepsilon\Phi_{zz}^{00}\Phi_y^{01} - 2\alpha\varepsilon\Phi_{yz}^{00}\Phi_z^{01} - \alpha\varepsilon\Phi_y^{00}\Phi_{zz}^{01} \\ & - 2\alpha\varepsilon\Phi_z^{00}\Phi_{yz}^{01} - \mathcal{F}^{-1} \left\{ -\frac{e^{-|\kappa|z}}{|\kappa|} \mathcal{F} \left[ \varepsilon\tilde{\Phi}_{yz}^1 \Big|_{z=0} \right] \right\} - \mathcal{F}^{-1} \left\{ -|\kappa|e^{-|\kappa|z} \mathcal{F} \left[ \varepsilon\tilde{F}^1 \Big|_{z=0} \right] \right\} \end{aligned} \quad (54a)$$

$$\begin{aligned} v = & \alpha\Phi_x^{01} + \alpha\varepsilon\Phi_{zz}^{00}\Phi_x^{01} + 2\alpha\varepsilon\Phi_z^{00}\Phi_{xz}^{01} - \mathcal{F}^{-1} \left\{ -|\kappa|e^{-|\kappa|z} \mathcal{F} \left[ \varepsilon\tilde{G}^1 \Big|_{z=0} \right] \right\} \\ & + \mathcal{F}^{-1} \left\{ -\frac{e^{-|\kappa|z}}{|\kappa|} \mathcal{F} \left[ \varepsilon\tilde{\Phi}_{xz}^1 \Big|_{z=0} \right] \right\}, \end{aligned} \quad (54b)$$

where

$$\tilde{F}^1 = -\mathcal{F}^{-1} \left\{ e^{-|\kappa|z} \mathcal{F} \left[ \left( \Phi_y^{00}\Phi_z^{00} + \alpha\Phi_z^{00}\Phi_y^{01} + \alpha\Phi_y^{00}\Phi_z^{01} \right) \Big|_{z=0} \right] \right\} \quad (54c)$$

$$\tilde{G}^1 = \alpha\mathcal{F}^{-1} \left\{ e^{-|\kappa|z} \mathcal{F} \left[ \left( \Phi_z^{00}\Phi_x^{01} \right) \Big|_{z=0} \right] \right\} \quad (54d)$$

$$\tilde{\Phi}^1 = -\mathcal{F}^{-1} \left\{ -\frac{e^{-|\kappa|z}}{|\kappa|} \mathcal{F} \left[ \left( \Phi_z^{00}\Phi_{zz}^{00} + \alpha\Phi_z^{01}\Phi_{zz}^{00} + \alpha\Phi_{zz}^{01}\Phi_z^{00} \right) \Big|_{z=0} \right] \right\}. \quad (54e)$$

At this stage, all  $O(\varepsilon)$  terms have been rewritten in terms of the SQG streamfunction using the diagnostic expressions derived in [6]. Every component in the full expansion is now solely a function of  $\Phi^{00}$  and  $\Phi^{01}$ .

Using the notation of this section, the basic state is

$$\Phi^{00} = \Psi_0 e^z \sin y. \quad (55a)$$

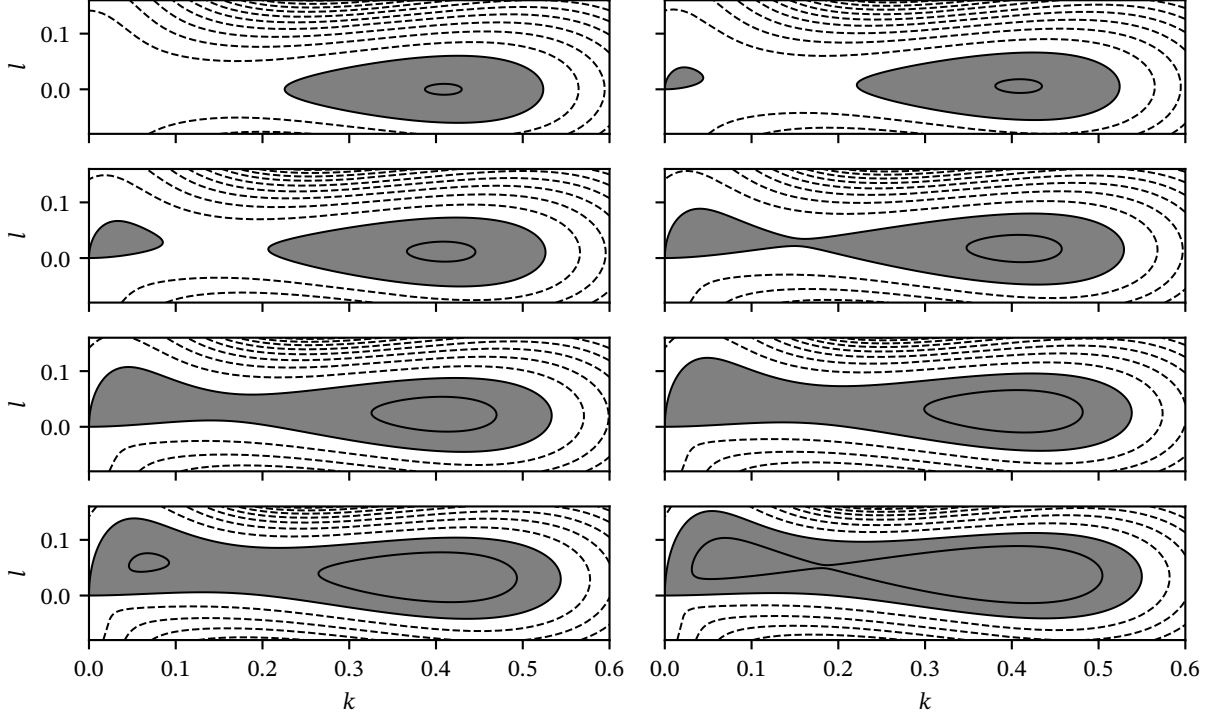


Figure 17: Growth rate diagrams for an SQG+ semi-infinite layer at various Rossby numbers.  $Re = 5$ . Left to right, top to bottom:  $\varepsilon = 0, 0.0571, 0.1143, 0.1714, 0.2286, 0.2857, 0.3429$  and  $0.4$ , with  $n = 1$  and  $\lambda = 0$ . The coupled equations are truncated at  $N = 16$ . The spacing between levels is  $0.004$ .

Treating the problem as a Floquet problem, we define

$$\Phi^{01} = e^{\sigma t + ikx + ily + \kappa z} \sum_{m=-\infty}^{\infty} \phi_m e^{imy}. \quad (55b)$$

Evaluating the expanded equation at  $z = 0$ , the linear growth rate of an SQG+ Kolmogorov system in a semi-infinite layer is governed by a recurrence relation,

$$\begin{aligned} \sigma \phi_m = & -\frac{\varepsilon k \Psi_0^2 (\kappa_{m+1} - \kappa_{m+2}) (\kappa_{m+1} - \kappa_{m+2} - 1) \phi_{m+2}}{4\kappa_{m+1}\kappa_m} + \frac{ik\Psi_0 (\kappa_{m+1} - 1) \phi_{m+1}}{2\kappa_m} \\ & + \frac{\varepsilon k \Psi_0^2 (\kappa_{m-1} - \kappa_{m-2}) (\kappa_{m-1} - \kappa_{m-2} - 1) \phi_{m-2}}{4\kappa_{m-1}\kappa_m} + \frac{ik\Psi_0 (\kappa_{m-1} - 1) \phi_{m-1}}{2\kappa_m} \\ & + \left( \frac{\varepsilon k \Psi_0^2 (\kappa_{m+1} - \kappa_{m-1}) (\kappa_{m+1}\kappa_{m-1} - \kappa_m^2 - \kappa_m)}{4\kappa_{m+1}\kappa_{m-1}\kappa_m} - \frac{\lambda + \kappa_m^{2n}}{Re} \right) \phi_m, \quad (56) \end{aligned}$$

where  $\kappa_m^2 = k^2 + (l + m)^2$  for clarity. With  $\varepsilon = 0$ , this reduces to the SQG recurrence relation (8).

Figure 17 shows the changes of the linear growth rate diagrams of a semi-infinite system with increasing Rossby number. The Reynolds number is chosen to be just above the SQG critical value. The introduction of ageostrophic corrections destroys the isotropy in wavenumber space. With  $\varepsilon \neq 0$ , the regions of instability in the  $k > 0$  half-plane are no longer symmetric about  $l = 0$ , but skews towards  $l > 0$ . Furthermore, as  $\varepsilon$  increases, a new region of instability develops near  $(k, l) = (0, 0)$ . As the Rossby number increases, the regions of instability visibly grow and they merge when  $0.11 < \varepsilon < 0.17$ . Simultaneously, the region of instability near  $(k, l) = (0, 0)$  becomes more unstable. At

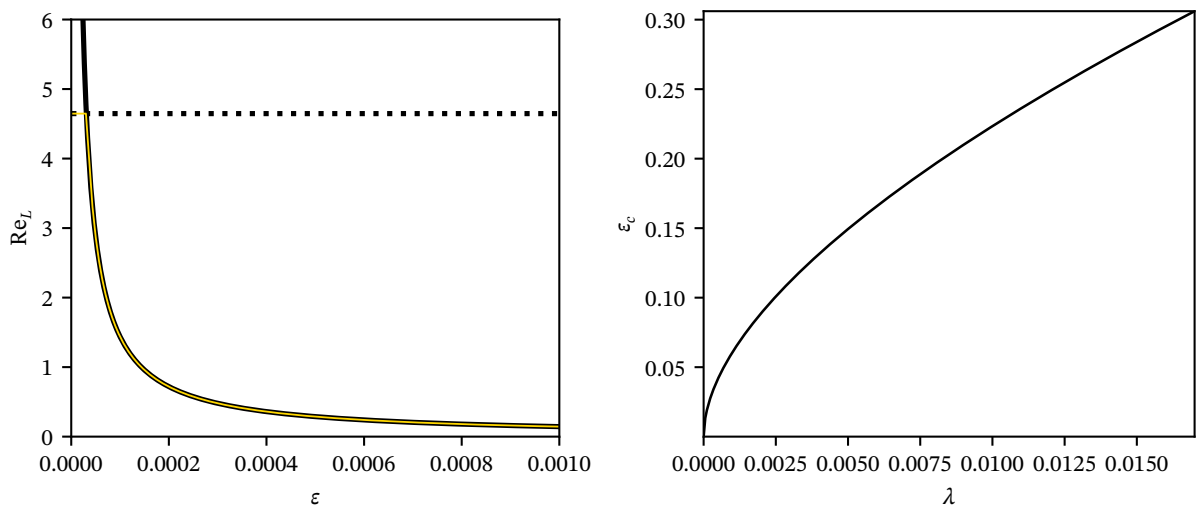


Figure 18: Left: critical Reynolds number vs.  $\varepsilon$ . The dashed black curve is the critical Reynolds number of the region of instability around  $k = 0.36$ . The solid black curve is the critical Reynolds number of the region of instability around  $k = 0$ . The two curves intersect at  $\varepsilon = 3.0957 \times 10^{-5}$ . The thin yellow curve in the first plot shows the effective critical Reynolds number as a function of  $\varepsilon$ . The intersection's relationship with damping is shown in the second plot.

$\varepsilon = 3.0957 \times 10^{-5}$ , this region of instability overtakes the region to its right to become the main destabilising modes of the system. The destabilising effect of the region of instability near  $(k, l) = (0, 0)$  is illustrated in the left panel of Figure 18. With zero damping and an increasing Rossby number, the critical Reynolds number drops rapidly at  $\varepsilon = 3.0957 \times 10^{-5}$ . By  $\varepsilon = 0.001$ , the linear critical Reynolds number of an SQG+ system is an order of magnitude lower than that of an SQG system. This effective critical Reynolds number is represented graphically by the thin yellow curve in the same plot. In other words, in the presence of ageostrophic effects, an SQG+ system is linearly unstable even with very strong viscous dissipation due to this long-wave instability.

The destabilising effect of ageostrophic corrections is easily counteracted by damping. The critical Rossby number at which this long-wave instability destabilises the system increases with the presence of damping and is shown as a function of  $\lambda$  in the right panel of Figure 18. In other words, the presence of small damping pushes the “cliff” in the critical Reynolds number shown in the left panel to much higher Rossby numbers. Figure 19 shows the growth rate diagrams with varying  $Re_c$  and  $\lambda$  at a fixed  $\varepsilon = 0.4$ . With increasing  $\lambda$ , the region of instability near  $(k, l) = (0, 0)$  is suppressed. While the growth rate diagrams are still anisotropic in wavenumber space, the regions of stability are approaching the teardrop shape of that of an SQG growth diagram. The stabilising power of damping is further demonstrated in Figure 20. The blue curve shows  $Re_c$  associated with the region of instability near the origin of the wavenumber space, whereas the orange curve shows  $Re_c$  of the region of instability to the right. As  $\lambda$  increases, the critical Reynolds number of the region of instability quickly increases, which indicates this region of stability is becoming more stable. By  $\lambda = 0.025$ , it is overtaken by the other centre of instability as the main destabilising mode.

The equivalent SQG curve is superposed on this graph. With small damping, an SQG system is more linearly stable than an SQG+ system. However, an SQG+ system stabilises more readily with increasing damping than an SQG system, and an SQG+ system is the more stable of the two with sufficiently large damping. Figure 21 shows the ratio of the critical Reynolds number for SQG+ over SQG systems with varying  $\varepsilon$  at large  $\lambda$ .

## 6. Discussion

In this paper, we have studied the linear and nonlinear stability of various SQG and SQG+ configurations using linearisation and the energy method. We have shown that, in contrast to a two-dimensional system, the initial linear destabilisation of a semi-infinite SQG system does not originate from the long wave limit. On the other hand, nonlinear analysis shows that  $k = 0$  remains the least stable mode, even with very strong damping.  $Re_{Ec}$  is 0 in the absence of

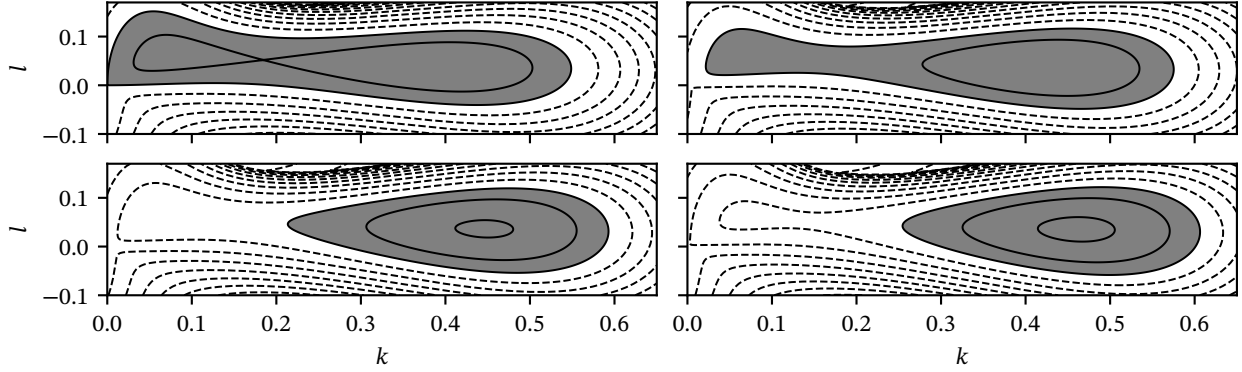


Figure 19: Growth rate diagrams for an SQG+ semi-infinite layer at  $\varepsilon = 0.4$ . The damping coefficient is, from left to right, top to bottom, 0, 0.0167, 0.033, and 0.05. These plots are all plotted at  $1.1Re_c(\varepsilon, \lambda)$  computed from the black, dotted curve in Figure 18, which are, in the same order, 4.530, 4.837, 5.089, and 5.318.

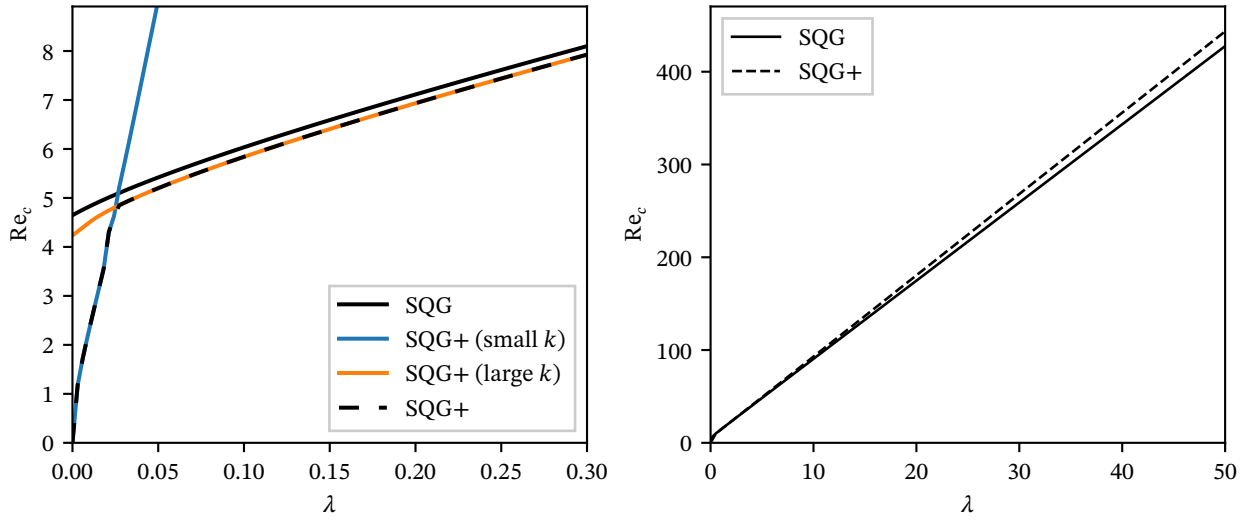


Figure 20: Linear critical Reynolds number plotted as a function of the damping parameter  $\lambda$ . The Rossby number is set to 0.4. As shown in Figure 17, there are two disconnected regions of instability in wavenumber space. The orange curve shows  $Re_c$  in  $k > 0.3$ , and the blue curve shows  $Re_c$  for the region the long length scale limit (small  $k$ ). The black dashed curve shows the effective critical Reynolds number. The curve representing the SQG critical Reynolds number is shown for comparison.

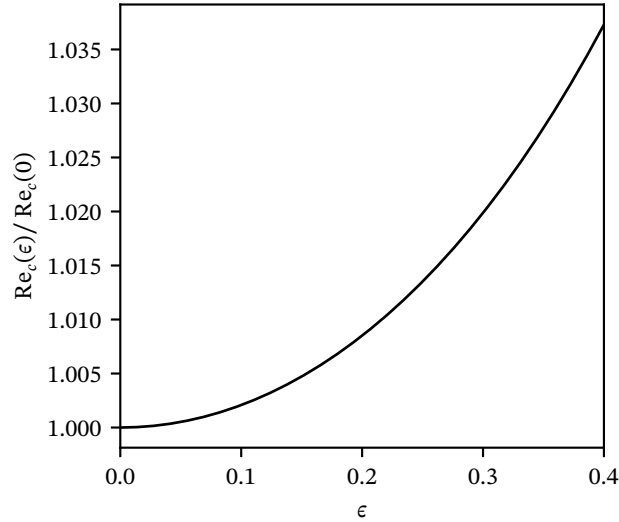


Figure 21: The slope of the SQG+ curve in Figure 20 as a function of the Rossby number at  $\lambda = 50$ . The results are normalised against the SQG result.

damping. With the increase of damping, the system becomes more stable. With sufficiently large damping, both the linear and nonlinear critical Reynolds number grow linearly with damping.

When an SQG system in a fluid layer of finite thickness is being forced from both the upper and lower boundaries, its behaviour is in between that of a semi-infinite SQG system and a 2D system: in a fluid layer with large enough thickness, the behaviour tends toward that of a semi-infinite SQG system, while for small thickness the behaviour of a symmetric configuration tends toward that of a 2D system. However, the antisymmetric configuration deviates from this pattern and becomes less prone to instability as the layer thickness is decreased, since the effects of the forcing on the two boundaries counteract one another in the fluid interior. Its nonlinear critical Reynolds number approaches infinity at the  $z_0 \ll 1$  limit. In the small depth limit, the hyperbolic sine function in (16a) approaches zero, and the boundary forcing essentially vanishes.

For a semi-infinite SQG+ system, we have also studied the impact of the ageostrophic corrections on stability. We found that in the absence of damping, the ageostrophic corrections greatly destabilise the system through instabilities in the long wave limit. The critical Reynolds number decreases rapidly as a region of instability develops near  $(k, l) = (0, 0)$ . We also found that this instability is very effectively tamed by the introduction of damping. Due to the enlargement of the regions of instability, an SQG+ system is more unstable than an equivalent SQG system when damping is weak. However, in the large damping regime, the opposite is true. We do not currently have a satisfactory explanation for this phenomenon.

While SQG is only a model for the ocean's submesoscale, the results of this paper suggest that the stability properties of an SQG system can be physically different from its 2D Euler counterpart. The dynamics will be dominated by physical processes that are noticeably smaller than the system length scale, unlike 2D Euler flows. The dynamics of an SQG system with two active layers depends on the thickness on the distance between the layers, a model for the oceanic mixed layer. A mixed layer that is thicker behaves more like a semi-infinite SQG system and a mixed layer that is sufficiently thin behaves more like a 2D Euler system. Our results with order Rossby corrections suggest that, under the influence of ageostrophic effects, instabilities originate from the eddies at the system length scale, more like a 2D system. However, the presence of drag shifts the dominant processes from the system length scale down to a smaller length scale. Between drag and ageostrophic effects lies rich physics that is worth exploring in future studies.

## Acknowledgements

The authors would like to acknowledge inspiring discussions with W. R. Young.

## CRediT

**Mac Lee:** Software, Formal analysis, Investigation, Writing - Original Draft **Stefan Llewellyn Smith:** Conceptualization, Methodology, Validation, Writing - Review & Editing, Supervision, Funding acquisition

## Funding

This research was partially funded by an ONR NISEC award through UCSD.

## Declaration of interests

The authors report no conflict of interest.

## References

- [1] W. Blumen, Uniform Potential Vorticity Flow: Part I. Theory of Wave Interactions and Two-Dimensional Turbulence, *J. Atmos. Sci.* 35 (5) (1978) 774–783. doi:10.1175/1520-0469(1978)035<0774:UPVFPI>2.0.CO;2.
- [2] I. M. Held, R. T. Pierrehumbert, S. T. Garner, K. L. Swanson, Surface quasi-geostrophic dynamics, *J. Fluid Mech.* 282 (1995) 1–20. doi:10.1017/S0022112095000012.
- [3] G. Lapeyre, P. Klein, Dynamics of the upper oceanic layers in terms of surface quasigeostrophy theory, *J. Phys. Oceanogr.* 36 (2) (2006) 165–176. doi:10.1175/JPO2840.1.
- [4] J. H. LaCasce, A. Mahadevan, Estimating subsurface horizontal and vertical velocities from sea-surface temperature, *J. Mar. Res.* 64 (2006) 695–721.
- [5] D. J. Muraki, C. Snyder, R. Rotunno, The next-order corrections to quasigeostrophic theory, *J. Atmos. Sci.* 56 (11) (1999) 1547–1560. doi:10.1175/1520-0469(1999)056<1547:TNOCTQ>2.0.CO;2.
- [6] G. J. Hakim, C. Snyder, D. J. Muraki, A new surface model for cyclone–anticyclone asymmetry, *J. Atmos. Sci.* 59 (16) (2002) 2405–2420. doi:10.1175/1520-0469(2002)059<2405:ANSMFC>2.0.CO;2.
- [7] N. F. Bondarenko, M. Z. Gak, F. V. Dolzhanskii, Laboratory and theoretical models of plane periodic flow, *Akademiia Nauk SSSR Fizika Atmosfery i Okeana* 15 (1979) 1017–1026.
- [8] J. M. Burgess, C. Bizon, W. D. McCormick, J. B. Swift, H. L. Swinney, Instability of the kolmogorov flow in a soap film, *Phys. Rev. E* 60 (1999) 715–721.
- [9] L. D. Meshalkin, I. G. Sinai, Investigation of the stability of a stationary solution of a system of equations for the plane movement of an incompressible viscous liquid, *J. Appl. Math. Mech.* 25 (6) (1961) 1700–1705. doi:10.1016/0021-8928(62)90149-1.
- [10] D. N. Beaumont, The stability of spatially periodic flows, *J. Fluid Mech.* 108 (1981) 461–474.
- [11] K. Gotoh, M. Yamada, J. Mizushima, The theory of stability of spatially periodic parallel flows, *J. Fluid Mech.* 127 (1983) 45–58. doi:10.1017/S0022112083002608.
- [12] G. Sivashinsky, V. Yakhot, Negative viscosity effect in large-scale flows, *Phys. Fluids* 28 (4) (1985) 1040–1042.
- [13] K. Gotoh, M. Yamada, The instability of rhombic cell flows, *Fluid Dyn. Res.* 1 (3) (1987) 165–176.
- [14] A. J. Manfroi, W. R. Young, Stability of  $\beta$ -plane kolmogorov flow, *Phys. D* 162 (3-4) (2002) 208–232.
- [15] Y.-K. Tsang, W. R. Young, Energy-entropy stability of  $\beta$ -plane kolmogorov flow with drag, *Phys. Fluids* 20 (8) (2008) 084102. doi:10.1063/1.2958321.

- [16] H. Fukuta, Y. Murakami, Nonlinear Stability of Kolmogorov Flow with Bottom-Friction Using the Energy Method, *J. Phys. Soc. Jpn.* 64 (10) (1995) 3725–3739. doi:10.1143/JPSJ.64.3725.
- [17] N. J. Balmforth, Y.-N. Young, Stratified kolmogorov flow, *J. Fluid Mech.* 450 (2002) 131–167. doi:10.1017/S0022111002006371.
- [18] B. Straughan, *The Energy Method, Stability, and Nonlinear Convection*, 2nd Edition, Applied Mathematical Sciences, Springer New York, NY, 2004. doi:10.1007/978-0-387-21740-6.
- [19] M. V. Kalashnik, M. V. Kurgansky, S. V. Kostykin, Instability of surface quasigeostrophic spatially periodic flows, *J. Atmos. Sci.* 77 (1) (2020) 239–255. doi:10.1175/JAS-D-19-0100.1.
- [20] M. V. Kalashnik, M. V. Kurgansky, O. G. Chkhetiani, Baroclinic instability of spatially-periodic flows in a discrete surface quasi-geostrophic model with two levels, *Dyn. Atmos. Oceans* 99 (2022) 101313. doi:10.1016/j.dynatmoce.2022.101313.